Fluorescent Magnetic Nanoparticles for Magnetically Enhanced Cancer Imaging and Targeting in Living Subjects

Aihua Fu,[†,§,‖,]* Robert J. Wilson,[†,§] Bryan R. Smith,[‡,§] Joyce Mullenix,[†,§] Chris Earhart,[†,§] Demir Akin,[‡,§] Samira Guccione,[‡] Shan X. Wang,[†,§,]* and Sanjiv S. Gambhir[‡,§,⊥,]*

[†]Department of Materials Science and Engineering, [‡]Department of Radiology, [§]Molecular Imaging Program at Stanford, and [⊥]Department of Bioengineering, Bio-X Program, Stanford University, Stanford, California 94305, United States and [‖]NVIGEN Inc., 265 Sobrante Way, Suite H, Sunnyvale, California 94086, United States

Many biological barriers in the body preclude systemically administered imaging contrast agents and drugs from reaching their target cells.[1] Even for agents with surface targeting molecules,[2] the cancer cell uptake is often much less than that of nonspecific accumulation. Many cancer drugs also reach other healthy parts of the body, including the heart, and can cause undesirable side effects.[3,4] Magnetic targeting has been proposed for decades to help direct drugs to localized sites.[5−7] Although conceptually very simple, magnetic targeting faces many technical challenges including the fast decay of the magnetic field gradient away from the magnet which reduces available magnetic force and limits magnetic targeting to superficial tissues;[5−7] thus the use of clusters of magnetic nanoparticles or cells loaded with many magnetic nanoparticles is required.[5−11] Here, we report a novel approach for magnetic targeting of individual magnetic nanoparticles containing a single 8 nm superparamagnetic iron oxide (SPIO) core in mouse subcutaneous xenograft models. We utilized a combination of an external permanent magnet to produce a moderate magnetic field and an embedded magnetizable micromesh to produce very strong magnetic field gradients that can simultaneously attract individual magnetic nanoparticles to multiple locations of the mesh. Provided that the magnetic fields are large enough to nearly saturate the mesh and nanoparticle moments, large magnetic field gradients are key to large magnetic forces, due to the dipole character of magnetic moments. Our targeting scheme allows generating modest (∼0.1 T) fields but

ABSTRACT
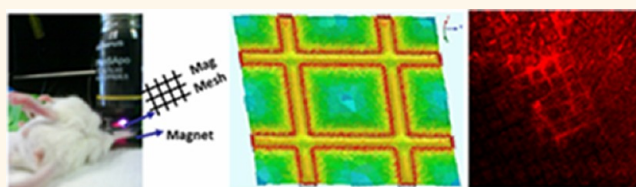
Early detection and targeted therapy are two major challenges in the battle against cancer. Novel imaging contrast agents and targeting approaches are greatly needed to improve the sensitivity and specificity of cancer theranostic agents. Here, we implemented a novel approach using a magnetic micromesh and biocompatible fluorescent magnetic nanoparticles (FMN) to magnetically enhance cancer targeting in living subjects. This approach enables magnetic targeting of systemically administered individual FMN, containing a single 8 nm superparamagnetic iron oxide core. Using a human glioblastoma mouse model, we show that nanoparticles can be magnetically retained in both the tumor neovasculature and surrounding tumor tissues. Magnetic accumulation of nanoparticles within the neovasculature was observable by fluorescence intravital microscopy in real time. Finally, we demonstrate that such magnetically enhanced cancer targeting augments the biological functions of molecules linked to the nanoparticle surface.

with large magnetic field gradients for magnetic actuation of single SPIOs, with actuation being an extremely challenging process due to small nanoparticle magnetic moments[8,12] and, to the best of our knowledge, has never been demonstrated in a living subject. Developing such techniques is extremely meaningful as it pushes the boundary of the size and distance limitation of traditional magnetic targeting and could lead to better use of this technique in the clinic. We demonstrate, by direct
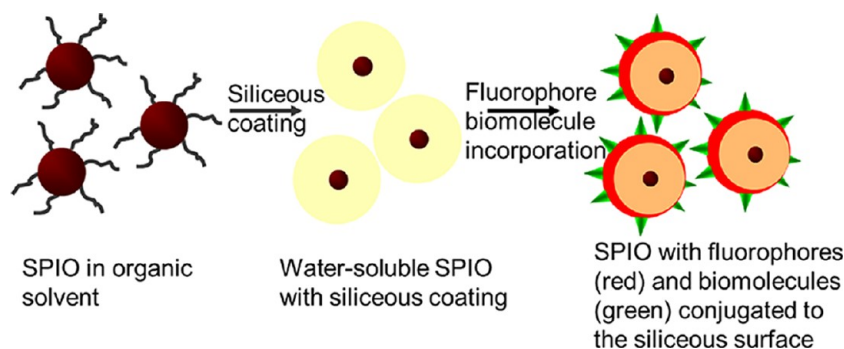
Scheme 1. Schematic illustration of the preparation of multifunctional nanoparticles with an individual SPIO core, a siliceous coating, and conjugated fluorophores and biomolecules.

observation under an intravital microscope, that such magnetic micromesh retained fluorescent magnetic nanoparticles (FMNs) while they are still in the cancer neovasculature or after extravasation. In addition, when using tumor angiogenic target $\alpha_v\beta_3$ integrin and its antagonist arginine-glycine-aspartic acid (RGD) as a model system,[13,14] our results show that magnetic targeting of RGD-loaded FMNs enhances their biological functions. In the human glioblastoma U87MG mouse subcutaneous xenograft model we used, tumor regression occurred more rapidly when using magnetic targeting (tumor signal decay half-life = 0.853 days, $n = 3$), as compared to FMN-RGD alone (tumor signal decay half-life = 6.197 days, $n = 3$) (Student's t test analysis, $n = 3$, $p < 0.05$).

RESULTS AND DISCUSSION

Although nanoparticles synthesized through both physical fabrication and wet chemistry have demonstrated ever increasing diversity and complexity,[15] nanoparticles suitable for clinical translation are rare. In this paper, the development of the nanoparticle platform is based on multifunctional fluorescent magnetic nanoparticles incorporating potentially biocompatible components. These nanoparticles each contain an SPIO core, the same material as in the clinical MRI agent Feridex and the colloidal iron oxide for treating iron deficiency anemia.[16] They are coated with a biocompatible siliceous shell, the material component similar to that used in daily calcium supplements. The fluorescence is from covalently bonded organic fluorophores, and FDA-approved fluorophores are available.[17]

Scheme 1 illustrates the general approach in preparing FMNs. Starting from SPIO cores, a silanization shell is first grown and then covalently linked to organic fluorophores, along with biofunctional molecules such as drugs or targeting molecules. The fluorescence of the particles permits direct imaging of the particles in a living subject through an intravital microscope, while the magnetic properties are suitable for magnetic targeting. As shown in the transmission electron micrograph of Figure 1A, for nanoparticles

deposited onto the TEM grid from a ready to inject solution, FMNs contain individual SPIO cores and remain well-dispersed. Dynamic light scattering (DLS) measurement demonstrated that the size of silanized SPIO is 87 nm (Supporting Information, Supplementary Figure 1). Since FMNs made by Cy5.5 fluorophore incorporation, as used in this study, have an emission wavelength interfering with the red laser used for DLS measurement, sizes of FMN-Cy5.5 nanoparticles cannot be directly measured using DLS. However, measurement of FMN samples that incorporate green fluorophores demonstrated that incorporation of fluorophores increased the nanoparticle size by 10 nm, so a rough estimation of the size of FMN-Cy5.5 utilized in this paper is 97 nm. When such nanoparticles are systemically administered in a mouse cancer model, the fluorescence from FMN allows high-resolution fluorescent imaging of the tumor neovasculature. As shown in Figure 1B, no aggregates of nanoparticles in the bloodstream were observed using optical microscopy and the FMN fluorescent signal smoothly outlines the tortuous tumor neovasculature, including the very thin capillaries that are only a few micrometers in diameter.

The strong fluorescence from these FMNs permits direct observation of their response under an external magnetic control in a living subject. Magnetic targeting can improve specific localization of nanoparticles when sufficient magnetic gradients are applied. This additional applied force can, in principle, help to overcome forces drawing particles away, such as viscous flow forces and other biological barriers,[1] and help to retain FMNs before RES uptake or nonspecific binding, after systemic administration. Magnetic targeting has been developed for many uses,[5−8,12] but magnetic targeting of individual nanoparticles with single SPIO cores in living subjects is extremely desirable for using small nanoparticles that can better escape the RES and penetrate tumors. This goal is challenging because a large magnetic field gradient is needed to generate a sufficient magnetic force which requires close proximity between magnets and nanoparticles since attainable magnetic field gradients fall off very rapidly with
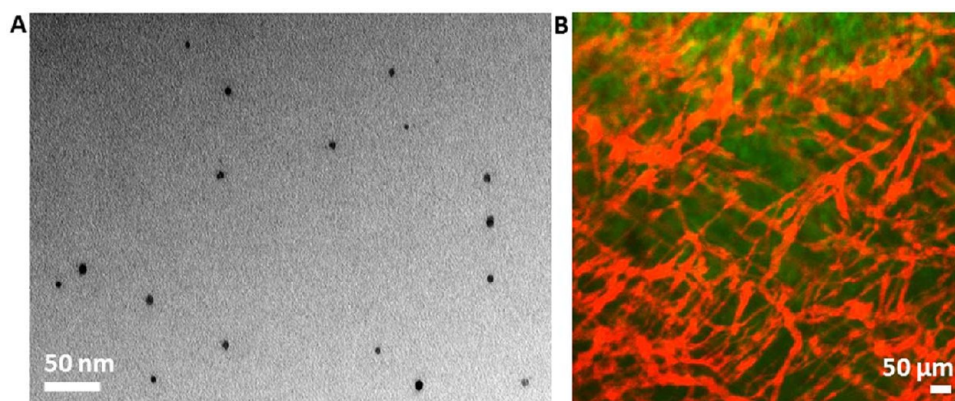
Figure 1. Injectable multifunctional fluorescent magnetic nanoparticles (FMNs). (A) Transmission electron micrograph showing FMNs with an individual SPIO core. **(B)** Overlaid image showing the red fluorescence from systemically administered FMNs outlining tumor neovasculature and the green color showing EGFP-transfected human U87MG glioblastoma tumor cells.
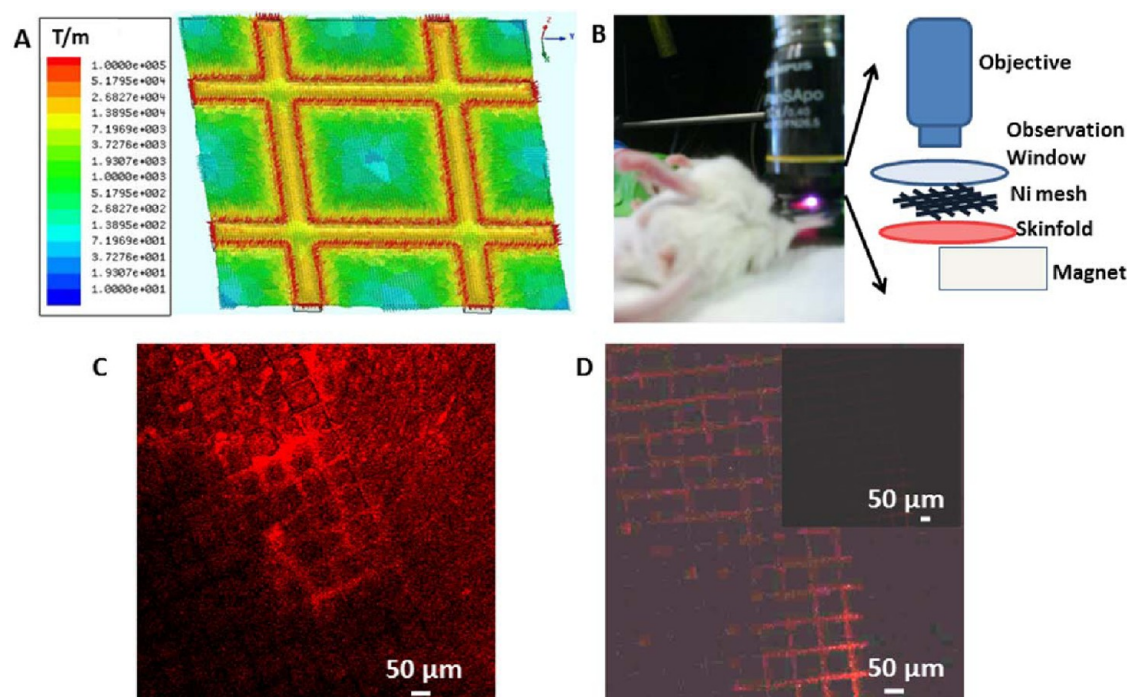

Figure 2. Maxwell simulation of the magnetic field gradient for the Ni micromesh and magnetic targeting of extravasated FMN. (A) Magnetic field gradient graph as calculated using Maxwell. The mesh pitch is 76 μm, and the magnetic field gradient is in T/m. **(B)** Experimental setup for magnetic targeting. **(C)** Extravasated nanoparticles are adsorbed to the Ni micromesh showing red fluorescence. The image was taken 106 min after induction of the magnetic force and 152 min after nanoparticle injection. Please note that on regions of the mesh where few FMNs were accumulated, the grid fluorescence is weak. **(D)** Control experiment shows negligible fluorescence signal from the mesh. Under the same imaging condition as in C, the whole field of view is dark, as shown in the inset. The brightness and contrast of main image in D is enhanced to display the grid outline and its weak, more uniform fluorescence.

distance. To ameliorate this limitation, we implemented an embedded magnetic micromesh that, when magnetized, can generate large magnetic field gradients distributed across a broad spatial range simultaneously. Although the use of two magnetic sources was previously applied for capturing large micrometer or submicrometer SPIO aggregates,[18] such a method has never been exploited to magnetically localize individual SPIO or demonstrated in living subjects. Figure 2A shows the magnitude and distribution of

the magnetic field gradient of an electroformed Ni micromesh under a perpendicular magnetic field of 2 kOe, as calculated using Maxwell simulation. Ni was chosen as these meshes are readily commercially available to serve as a model for more biocompatible, magnetizable grids. A permanently magnetized mesh might also allow the elimination of the external magnet while retaining the high gradient, but the biocompatibility of permanent magnet materials is less likely than for magnetizable materials. The Ni mesh has a

76 μm pitch, 12 μm wire width, and 5 μm wire thickness. The simulation shows that large magnetic field gradients of 10^4 to 10^5 T/m are generated within 10 μm of the Ni wire edges. Under such large gradients, the magnetic forces exerted on single 8 nm SPIO cores within this proximity are large enough to overcome the viscous drag on nanoparticles within tumor vasculature (see supplementary calculation). The field gradients from the external permanent magnet used to magnetize the mesh are much smaller, 10 T/m, and cannot exert forces large enough to accumulate FMNs. The experimental setup is illustrated in Figure 2B. The Ni micromesh is placed directly on the surface of the tumor in the DSC window. The permanent magnet, with field strength of 2 kOe and a maximum field gradient of 10 T/m near the surface, is placed underneath the DSC window and magnetizes both the Ni mesh and FMNs in the tumor vasculature.

The power of this setup lies in the combined use of two magnetic entities to eliminate the dilemma related to attaining a large magnetic field gradient while maintaining a relatively large distance from a bulky external magnet. With this scheme, the ultrathin magnetizable micromesh can be inserted at the tumor location to generate a large gradient, while the permanent magnet, used to magnetize the micromesh and magnetic nanoparticles, can be placed farther away from the magnetic targeting site. In our experimental setup, the magnetized Ni micromesh generates forces which are large enough to capture FMNs. Figure 2C shows that FMNs accumulated at the edges of Ni wires near vasculature and that extravasated FMNs outline the mesh microstructure with red FMN fluorescence, as expected from the simulated magnetic field gradient distribution of the micromesh. In the control experiment, when only the magnetic mesh was imaged under identical imaging conditions and directly displayed without any intensity adjustment, the signal of the mesh itself is almost negligible. To display the mesh outline from its intrinsic weak fluorescence, as shown in Figure 2D, the image brightness and contrast have to be adjusted, with the inset image showing the weak fluorescence using the intensity scale as Figure 2C. In Figure 2C, the fluorescence from the mesh is highly variable over the image, indicating that the fluorescence from brighter regions is not associated with the bare Ni mesh background. On regions of the mesh where few FMNs were accumulated, the grid fluorescence is weak, and regions with varying FMN accumulation have variations in apparent width and brightness. All of these features indicate that the red color on the mesh in Figure 2C is not from the mesh fluorescence itself, but rather from the accumulated FMNs.

This experimental setup is also able to magnetically retain FMNs within tumor neovasculature. Figure 3A shows images from three channels that detect FMN fluorescence in red, Angiosense (circulating dye) fluorescence in blue, and EGFP tumor signal in green. This figure also shows the outline of regions of interest (ROI) that were specified and tracked for all of the imaging frames in three videos, as an aid for quantitative analysis. These videos are provided in the Supporting Information; each contains 60 image frames recorded at 10 s intervals, beginning 4 min after exerting the magnetic force and spanning 10 min. The average intensity of each ROI was calculated using ImageJ and plotted in Figure 3B, where it is clear that the average intensity of the FMN signal in the ROI continuously increases throughout the 60 imaging frames and over the 10 min time interval. The real-time accumulation of FMNs under the magnetic targeting can be directly observed in the supplementary movies, and the increase in average intensity over the ROI comes mostly from an increased fluorescent area, rather than increasing peak intensity. On the other hand, the Angiosense and the tumor GFP signals show negligible increases in average intensity over ROI with time. The specific vessel shown here may be at the end of a tumor neovascular sprout, which is often located at the top of the tumor mass and is hence closest to the Ni micromesh and its strong magnetic field gradient.

Successful magnetic retention of FMNs can also be observed within the well-developed neovasculature. In Figure 3C, the image channels for Angiosense (left panel, blue color) and FMN (right panel, red color) are placed side by side for comparison. For tumor neovasculature at the center of the image, which is outlined in a relatively consistent manner by Angiosense, punctate nodal spots at edges of Ni wires are obvious in the FMN signal channel. This is because the strong magnetic forces from the edges of Ni wires are able to retain FMNs, resulting in stronger fluorescence signal at the nodal spots. The ratio of averaged FMN fluorescence intensities for a ROI that encircles the nodal spot at the Ni wire edge *versus* that from a ROI that encloses the vessel area near the center of the Ni mesh hole is much larger than that for the Angiosense channel. A few pairs of such locations are indicated using colored arrows in Figure 3C. Corresponding intensity ratios for each pair are shown in the table of Figure 3D, along with a bar graph of the average values and standard deviations. The average intensity ratio for FMN signal is five times that of Angiosense signal. This clearly demonstrates that FMNs were able to respond to the external magnetic field gradient generated by the Ni micromesh and thus magnetically accumulated close to the wire edge to form nodal spots with intense fluorescence.

The magnetic targeting of FMN to the tumor region could largely impact the functions of biomolecules
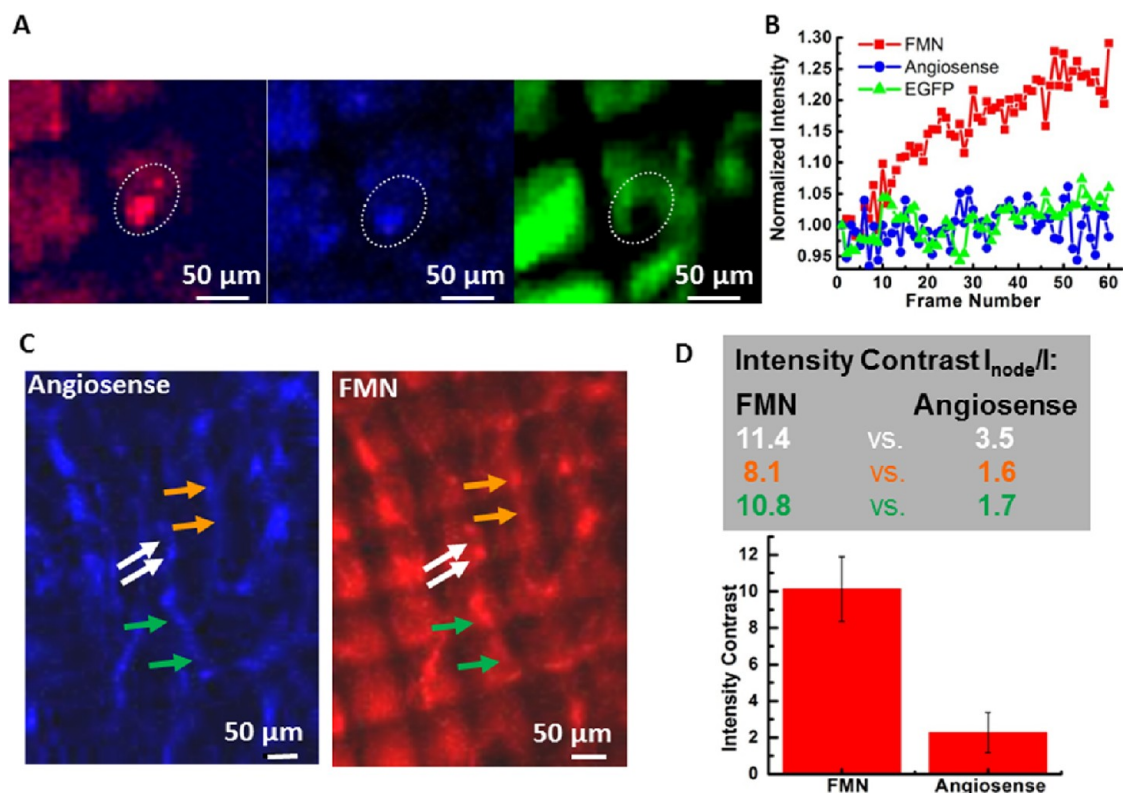
Figure 3. Magnetic targeting of FMN within tumor neovasculature. (A) Real-time observation of magnetic accumulation of FMNs to the mesh edge. The three image channels are as follows: red for FMN fluorescence, blue for Angiosense 750 fluorescence, and green for EGFP-transfected tumor signal. Each image represents the first frame of 60 frame movies capturing a 10 min magnetic targeting event starting 4 min after applying the magnetic force. Corresponding movies are shown in the Supporting Information. (B) Intensity change with frame number for the ROIs outlined using the white dash in (A). (C) Angiosense 750 channel (blue) and the FMN channel (red) imaged 20 min after activating the magnetic field. (D) Top: Intensity contrast for ROIs that circle the nodal spot at the Ni wire edge *versus* that enclosing the vessel area near the center of the Ni mesh hole for FMN (number on the left) and Angiosense (right). The color of the number corresponds to the color of arrows in C. Bottom: Bar graph represents the average intensity contrast and its standard deviation for the FMN and the Angiosense channels.
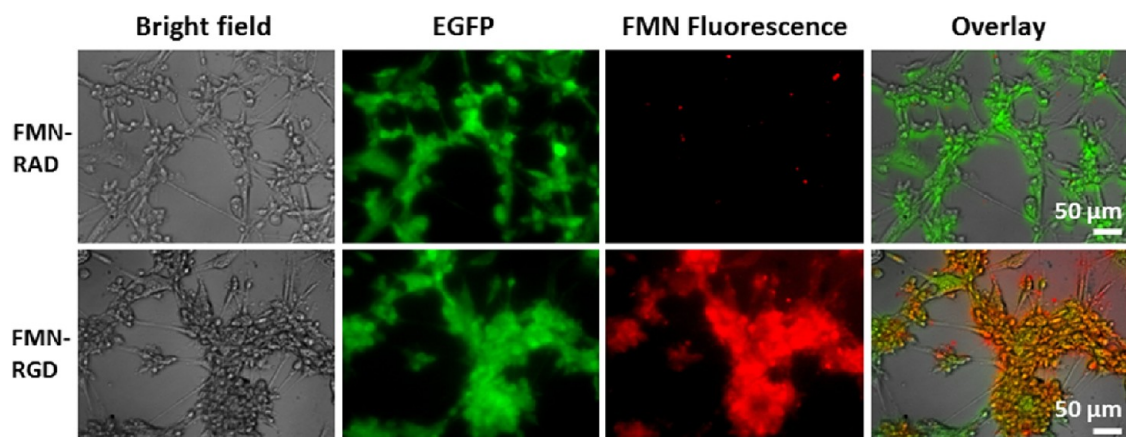

Figure 4. Cell staining experiments demonstrate binding specificity of FMN-RGD to cultured U87MG human glioblastoma cells in comparison with FMN-RAD. U87MG cells overexpress $\alpha_v\beta_3$ integrin on the cell surface and RGD peptide binds to it. U87MG cells are transfected with EGFP and show green fluorescence. FMNs are coated with Cy5.5 and hence have red fluorescence that can be detected under a fluorescence microscope.

conjugated to FMN surfaces. Here we used RGD binding to tumor angiogenic target $\alpha_v\beta_3$ integrin as a model system, which is reported to cause apoptosis of tumor blood vessels and promote tumor regression.[13] The scrambled form RAD (Arg-D-Ala-Asp)[19] was

utilized in control experiments. FMN-RGD demonstrated binding specificity to cultured U87MG human glioblastoma cells, as compared to FMN-RAD (Figure 4). For experiments in living subjects, we selected the intensity of the tumor EGFP signal to monitor the
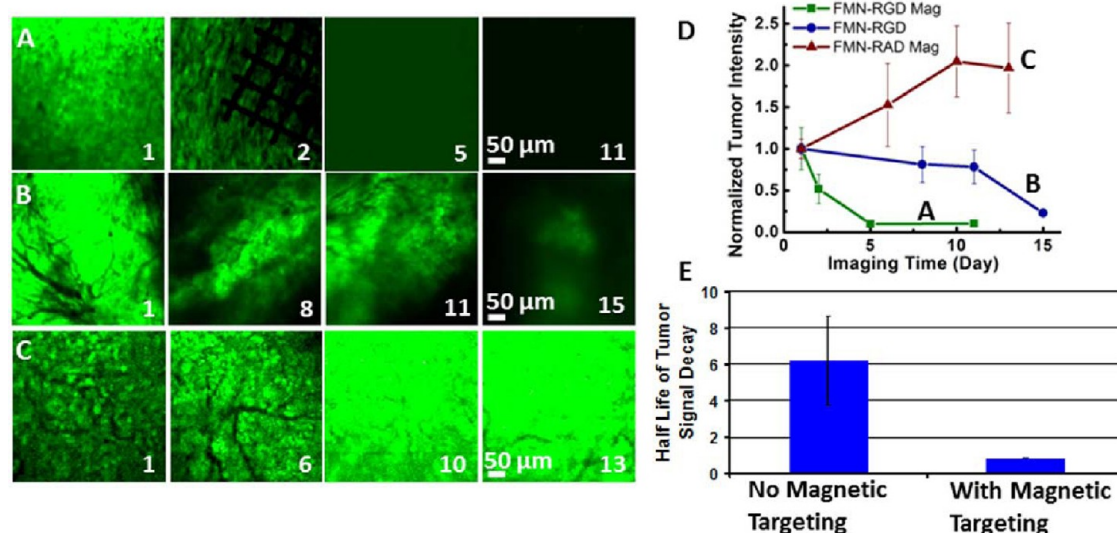
Figure 5. RGD-conjugated FMNs in combination with external magnetic control accelerates tumor regression in a U87MG human glioblastoma xenograft mouse model. (A−C) EGFP-transfected tumor image channels show tumor intensity change within days of imaging for FMN-RGD together with magnetic targeting (A), FMN-RGD without magnetic targeting (B), and FMN-RAD under magnetic targeting (C). Day 1 is the day of FMN injection and magnetic targeting. The permanent magnet was placed for 2 h, and the Ni micromesh was removed the following day to better observe the imaging area. **(D)** Normalized tumor intensity *vs* imaging time curves demonstrate that FMN-RGD together with magnetic targeting can expedite tumor regression ($n = 3$, $P < 0.05$). The fluorescence image intensity scales were set so that the brightest image within each series (A−C) was near saturation. **(E)** Half-lives of tumor fluorescence signal decay demonstrate significantly faster tumor regression for FMN-RGD injection with magnetic targeting ($n = 3$, ∼1 day) compared to without magnetic targeting ($n = 3$, ∼6 days). The half-lives were obtained by fitting each of the six FMN-RGD injection curves (Figure 5D and Supporting Information Supplementary Figure 3) to a first-order exponential decay function.

RGD-induced effects in different experiments since nanoparticles could extravasate out of leaky tumor vessels and remain in tumor regions for extended time regardless of surface molecular specificity, in line with the enhanced permeability and retention effect of nanoparticles.[20,21] Figure 5 shows that intravenously injected FMN-RGD caused tumor regression ($n = 3$), while tumors continued to grow after FMN-RAD injection ($n = 2$). For FMN-RGD injection together with magnetic targeting, tumors regressed at a much faster pace (tumor signal decay half-life of 0.853 days) than when injecting FMN-RGD without any magnetic force with a tumor signal decay half-life of 6.197 days ($n = 3$, $p < 0.05$, Figure 5A,B,E and Supporting Information Supplementary Figures 2 and 3). The tumor signal decay pattern under magnetic targeting is similar to that obtained by doubling the FMN-RGD dosage (Supplementary Figures 2 and 3), suggesting that expedited tumor regression under magnetic targeting is due to the retention of more FMN-RGD in the tumor region by virtue of magnetic targeting. More rigorous dosage experiments will need to be eventually performed to exactly quantify the dose equivalence of the magnetic targeting scheme.

CONCLUSION

FMNs present a multitude of nanoparticle characteristics that can be used to improve the current state

of the art in cancer molecular imaging and targeting. They can be formulated as multifunctional agents that offer imaging and molecular targeting functions, while also allowing externally enhanced nanoparticle localization in living subjects through the use of magnetic forces. Our *in vivo* magnetic targeting approach developed here enables manipulation of individual nanoparticles with single 8 nm SPIO cores, which has been a formidable challenge in many magnetic targeting experiments. The approach presented here opens the doors for utilization of individual SPIO nanoparticles, a proven biocompatible nanoparticle form, for magnetically enhanced targeting and imaging applications in living subjects. This system can be further developed by making the magnetic micromesh biodegradable,[22] for example, by utilizing meshes of SPIO materials in a biodegradable polymeric fibrous framework and by using multiple micromeshes to enclose or segregate tumor mass and capture drug-loaded FMNs at the tumor sites. The combined magnetic micromesh and nanoparticle procedures can improve cancer therapy through the fine control over the targeting and administration of both systemic and localized anticancer therapy modalities and serve as an alternative minimally invasive procedure to surgical tumor removal. Although rigorous experimentation and preclinical evaluation are still required prior to their clinical use, active development

of these FMNs and similar approaches are urgently needed for realization of nanotechnology-based solutions for challenging biomedical problems, such as earlier cancer detection and targeted therapy.[23]

EXPERIMENTAL METHODS

FMN Preparation. SPIOs were synthesized by oxidative decomposition of iron pentacarbonyl in trimethylamine oxide, oleic acid, and hexadecane.[24] The average particle size is 8 nm, as measured by transmission electron microscopy (TEM) (Supplementary Figure 4). Afterward, silanization coating chemistry was developed to render SPIO water-soluble and biocompatible. Briefly, mercapto/aminopropyl trimethoxyl silane was added to coat the surface of SPIO by forming a cross-linked shell under basic conditions using tetramethylammonium hydroxide as the base in a methanol solution. By adjusting the quantity of silane molecules added, the shell thickness can be controlled. In this work, the size of silanized SPIO before fluorophore incorporation is 87 nm as measured by dynamic light scattering technique, which implies a silanization coating thickness of roughly 40 nm. Both mercapto and amino groups are incorporated onto the nanoparticle surface. Near-infrared fluorophores (Cy5.5) with NHS (N-hydroxysulfosuccinimide) modification (GE Healthcare) are covalently bonded to the amino groups. A small cyclo[Arg-Gly-Asp-D-Tyr-Lys] (RGD) that can specifically target tumor angiogenesis marker $\alpha_v\beta_3$, or its inactive control peptide cyclo[Arg-D-Ala-Asp-Tyr-Lys] (RAD), was bound to mercapto groups of the silanized SPIO surface using a cross-linker sulfo-SMCC (sulfosuccinimidyl 4-[N-maleimidomethyl]cyclohexane-1-carboxylate, Thermo Fisher Scientific).

FMN Characterization. Transmission electron microscopy (TEM) imaging and characterization was performed using a JEOL TEM1230 at 80 kV. Dynamic light scattering was performed on a ZetaPlus analyzer (Brookhaven Instruments Corporation).

Animal Experiments. These were conducted in accordance with the ethical guidelines of the National Institutes of Health and with the approval of the Institutional Animal Care and Use Committee of Stanford University.

Intravital Imaging. This was performed using an IV-100 intravital microscope (Olympus, Center Valley, PA). The experimental preparation included the following: (1) surgically implant a dorsal skinfold chamber (DSC, APJ Trading Co., Inc., Ventura, CA) onto the back of the SCID mouse (Charles River, Wilmington, MA) which is a retired male breeder weighing more than 28 g, and wait for 2–3 days; (2) 1 million EGFP-transfected U87MG human glioblastoma cells were inoculated in low volume of 20 μL directly on top of the skinfold in the DSC. Tumor was allowed to grow for 10 days before imaging. On the day of intravital imaging, the mouse was anesthetized with isoflurane and positioned with the DSC fixed beneath the 10× objective of the intravital microscope. Commercial vascular dye Angiosense 750 (VisEn Medical, Woburn, MA) and FMN (with RGD or RAD) were subsequently injected into the mouse tail vein. Laser sources at 488, 633, and 748 nm were used for excitation. Three corresponding output channels illustrated in this paper with green for the EGFP-transfected tumor, red for FMN-Cy5.5, and blue for Angiosense 750 were simultaneously scanned for image acquisition. Resolutions of 320 and 512 pixel were selected in most imaging situations. The injection amount of Angiosense is 100 μL of original solution, which corresponds to 1.3 nmol of Angiosense. The FMN concentration was kept at 0.1 μM. A 100 μL solution of FMN (10 pmol) was injected for most experiments except for the dosage experiments, where 200 μL (20 pmol) of FMN was injected. Intravital imaging permits direct observation of the behavior of FMN in living subjects.

Magnetic Targeting. The observation of magnetic nanoparticle accumulation *in vivo* was accomplished using an intravital microscope and a tumor xenograft mouse model in a dorsal skinfold chamber (DSC). For a general experiment, EGFP-transfected U87MG human glioblastoma cells ($\sim$1 × 10^6) were inoculated and grown on the back of one mouse, and inside the DSC, for 10 days. Then commercial vascular dye Angiosense 750 and FMN (with RGD or RAD) were intravenously injected, both of which outline the tumor neovasculature. The tumor area and tumor neovasculature were examined using intravital microscopy after the injection of Angiosense and FMN. Because tumor vascular growth is heterogeneous, including variations of the depth and separation of vessels, an area with the best vessel structure in the entire observation window is selected. Then a small piece (edge length $\sim$3–8 mm) of electroformed Ni micromesh (wire width 12 μm and thickness 5 μm) was placed on top of the area. The magnetic force began when a permanent NdFeB N52 rectangular bar magnet (7.5 × 7.5 × 22 mm^3) was placed beneath the DSC window on the back side of the skinfold. The permanent magnet has a field strength of 2 kOe and a maximum field gradient of 10 T/m near the surface.

Statistical Analysis. The statistics for magnetic targeting (Figure 3D) were obtained from the average and standard deviation of fluorescence intensity ratios corresponding to the three pairs of colored arrows. The statistical analysis for tumor signal change with time of FMN-RGD, FMN-RAD, and magnetic targeting (Figure 5D) was based on the intensity of eight ROIs from two representative images of each imaging time point. The ROIs were selected to be within regions with the brightest tumor (EGFP) signals. The statistical analysis of the half-lives of tumor signal decay (Figure 5E) was generated by fitting each of the six FMN-RGD injection curves (Figure 5D and Supplementary Figure 3), three for injection under magnetic targeting, and three for injection without magnetic targeting, to a first-order exponential decay function. The statistically different tumor signal decay trends were confirmed by a Student's *t* test analysis of FMN-RGD injections with and without magnetic targeting (n = 3, p < 0.05).

REFERENCES AND NOTES

1. Sanhai, W. R.; Sakamoto, J. H.; Canady, R.; Ferrari, M. Seven Challenges for Nanomedicine. *Nat. Nanotechnol.* **2008**, *3*, 242–244.

2. Liu, Z.; Cai, W.; He, L.; Nakayama, N.; Chen, K.; Sun, X.; Chen, X.; Dai, H. *In Vivo* Biodistribution and Highly Efficient Tumour Targeting of Carbon Nanotubes in Mice. *Nat. Nanotechnol.* **2007**, *2*, 47–52.

3. Albini, A.; Pennesi, G.; Donatelli, F.; Cammarota, R.; Flora, S. D.; Noonan, D. M. Cardiotoxicity of Anticancer Drugs: The Need for Cardio-Oncology and Cardio-Oncological Prevention. *J. Natl. Cancer Inst.* **2010**, *102*, 14–25.

4. Force, T.; Krause, D. S.; Van Etten, R. A. Molecular Mechanisms of Cardiotoxicity of Tyrosine Kinase Inhibition. *Nat. Rev. Cancer* **2007**, *7*, 332–344.

5. Barnett, B. P.; Arepally, A.; Karmarkar, P. V.; Qian, D.; Gilson, W. D.; Walczak, P.; Howland, V.; Lawler, L.; Lauzon, C.; Stuber, M.; *et al.* Magnetic Resonance-Guided, Real Time Targeted Delivery and Imaging of Magnetocapsules Immunoprotecting Pancreatic Islet Cells. *Nat. Med.* **2007**, *13*, 986–991.

6. Meyers, P. H.; Cronic, F.; Nice, C. M., Jr. Experimental Approach in the Use and Magnetic Control of Metallic Iron Particles in the Lymphatic and Vascular System of Dogs as a Contrast and Isotopic Agent. *Am. J. Roentgenol. Radium Ther. Nucl. Med.* **1963**, *90*, 1068–1077.

7. Pankhurst, Q. A.; Thanh, N. K. T.; Jones, S. K.; Dobson, J. Progress in Applications of Magnetic Nanoparticles in Biomedicine. *J. Phys. D: Appl. Phys.* **2009**, *42*, 224001.

8. Dobson, J. Remote Control of Cellular Behavior with Magnetic Nanoparticles. *Nat. Nanotechnol.* **2008**, *3*, 139–143.

9. Cheng, K.; Li, T.-S.; Malliaras, K.; Davis, D.; Zhang, Y.; Marban, E. Magnetic Targeting Enhances Engraftment and Functional Benefit of Iron-Labeled Cardiosphere-Derived Cells in Myocardial Infarction. *Circ. Res.* **2010**, *106*, 1570–1581.

10. Namiki, Y.; Namiki, T.; Yoshida, H.; Ishii, Y.; Tsubota, A.; Koido, S.; Nariai, K.; Mitsunaga, M.; Yanagisawa, S.; Kashiwagi, H.; Mabashi, Y.; *et al.* Novel Magnetic Crystal-Lipid Nanostructure for Magnetically Guided *In Vivo* Gene Delivery. *Nat. Nanotechnol.* **2009**, *4*, 598–606.

11. Galanzha, E. I.; Shashkov, E. V.; Kelly, T.; Kim, J.; Yang, L.; Zharov, V. P. *In Vivo* Magnetic Enrichment and Multiplex Photoacoustic Detection of Circulating Tumour Cells. *Nat. Nanotechnol.* **2009**, *4*, 855–860.

12. Mannix, R. J.; Kumar, S.; Cassiola, F.; Montoya-Zavala, M.; Ingber, D. E. Nanomagnetic Actuation of Receptor-Mediated Signal Transduction. *Nat. Nanotechnol.* **2008**, *3*, 36–40.

13. Brooks, P. C.; Montgomery, A. M. P.; Rosenfeld, M.; Reisfeld, R. A.; Hu, T.; Klier, G.; Cheresh, D. A. Integrin Antagonists Promote Tumor Regression by Inducing Apoptosis of Angiogenic Blood Vessels. *Cell* **1994**, *79*, 1157–1164.

14. Janssen, M. L.; Oyen, W. J.; Dijkgraaf, I.; Massuger, L. F.; Frielink, C.; Edwards, D. S.; Rajopadhye, M.; Boonstra, H.; Corstens, F. H.; Boerman, O. C. Tumor Targeting with Radiolabeled $\alpha v \beta 3$ Integrin Binding Peptides in a Nude Mouse Model. *Cancer Res.* **2002**, *62*, 6146–6151.

15. Yin, Y.; Alivisatos, A. P. Colloidal Nanocrystal Synthesis and the Organic–Inorganic Interface. *Nature* **2005**, *437*, 664–670.

16. Wallerstein, R. O. Intramuscular Iron for the Treatment of Iron Deficiency Anemia in Infancy. *J. Pediatr.* **1956**, *49*, 173–176.

17. Alford, R.; Simpson, H. M.; Duberman, J.; Hill, G. C.; Ogawa, M.; Regino, C.; Kobayashi, H.; Choyke, P. L. Toxicity of Organic Fluorophores Used in Molecular Imaging: Literature Review. *Mol. Imaging* **2009**, *8*, 341–354.

18. Yellen, B. B.; Forbes, Z. G.; Halverson, D. S.; Fridman, G.; Barbee, K. A.; Chorny, M.; Levy, R.; Friedman, G. Targeted Drug Delivery to Magnetic Implants for Therapeutic Applications. *J. Magn. Magn. Mater.* **2005**, *293*, 647–654.

19. Smith, B. R.; Cheng, Z.; De, A.; Koh, A. L.; Sinclair, R.; Gambhir, S. S. Real-Time Intravital Imaging of RGD-Quantum Dot Binding to Luminal Endothelium in Mouse Tumor Neovasculature. *Nano Lett.* **2008**, *8*, 2599–2606.

20. Bartlett, D. W.; Su, H.; Hildebrandt, I. J.; Weber, W. A.; Davis, M. E. Impact of Tumor-Specific Targeting on the Biodistribution and Efficacy of siRNA Nanoparticles Measured by Multimodality *In Vivo* Imaging. *Proc. Natl. Acad. Sci. U.S.A.* **2007**, *104*, 15549–15554.

21. Smith, B. R.; Cheng, Z.; De, A.; Rosenberg, J.; Gambhir, S. S. Dynamic Visualization of RGD-Quantum Dot Binding to Tumor Neovasculature and Extravasation in Multiple Living Mouse Models Using Intravital Microscopy. *Small* **2010**, *6*, 2222–2229.

22. Litt, B.; Rogers, J. A. Dissolvable Films of Silk Fibroin for Ultrathin Conformal Bio-Integrated Electronics. *Nat. Mater.* **2010**, *9*, 2745.

23. Davis, M. E.; Zuckerman, J. E.; Choi, C. H. J.; Seligson, D.; Tolcher, A.; Alabi, C. A.; Yen, Y.; Heidel, J. D.; Ribas, A. Evidence of RNAi in Humans from Systemically Administered siRNA *via* Targeted Nanoparticles. *Nature* **2010**, *464*, 1067–1070.

24. Bonitatebus, J.; Acar, P. J.; Yagci, H. Method of Making Crystalline Nanoparticles. US 20040022937A1, EP1394223, 10/208,945.